Lopez Comino, J. A., Stich, D., Morales, J., Ferreira, A. M. G. (2016): Resolution of rupture directivity in weak events: 1-D versus 2-D source parameterizations for the 2011, Mw 4.6 and 5.2 Lorca earthquakes, Spain. - *Journal of Geophysical Research*, *121*, 9, pp. 6608—6626.

DOI: http://doi.org/10.1002/2016JB013227

AGU PUBLICATIONS

JGR

Journal of Geophysical Research: Solid Earth

RESEARCH ARTICLE
10.1002/2016JB013227

Key Points:
- We infer directivity from apparent source time functions and quantify the associated uncertainties
- We compare 1-D and 2-D source models for two M_w 4.6 and 5.2 earthquakes in 2011 near Lorca
- The direction SW and updip of both earthquakes could be inherent to this fault segment

Supporting Information:
- Supporting Information S1

Correspondence to:
J. A. López-Comino,
jalopez@gfz-potsdam.de

Citation:
López-Comino, J. A., D. Stich, J. Morales, and A. M. G. Ferreira (2016), Resolution of rupture directivity in weak events: 1-D versus 2-D source parameterizations for the 2011, M_w 4.6 and 5.2 Lorca earthquakes, Spain, *J. Geophys. Res. Solid Earth*, *121*, 6608–6626, doi:10.1002/2016JB013227.

Received 2 JUN 2016
Accepted 16 AUG 2016
Accepted article online 20 AUG 2016
Published online 17 SEP 2016

Resolution of rupture directivity in weak events: 1-D versus 2-D source parameterizations for the 2011, M_w 4.6 and 5.2 Lorca earthquakes, Spain

J. A. López-Comino[1,2], D. Stich[2,3], J. Morales[2,3], and A. M. G. Ferreira[4,5]

[1]GFZ German Research Centre for Geosciences, Potsdam, Germany, [2]Instituto Andaluz de Geofísica, Universidad de Granada, Granada, Spain, [3]Departamento de Física Teórica y del Cosmos, Universidad de Granada, Granada, Spain, [4]Department of Earth Sciences, Faculty of Mathematical and Physical Sciences, University College London, London, UK, [5]CERIS, Instituto Superior Técnico, Universidade de Lisboa, Lisbon, Portugal

Abstract Resolving robust source parameters of small-moderate magnitude earthquakes is still a challenge in seismology. We infer directivity from apparent source time functions (ASTFs) at regional distance and quantify the associated uncertainties. ASTFs are used for (i) modeling a propagating 1-D line source from the duration data and (ii) inverting the 2-D slip distribution from the full signals. Slip inversion is performed through a Popperian scheme, where random trial models are either falsified on account of large misfit, or else become members of the solution set of the inverse problem. We assess the resolution of rupture directivity representing centroid shifts from the solution set in a rose diagram. Using as example an event with well-studied rupture directivity, the 2011 M_w 5.2 Lorca (Spain) earthquake, 1-D and 2-D parameterizations yield similar estimates for direction (N213°E and N220°E, respectively) and asymmetry (67:33, 65:35) of rupture propagation, as well as rupture length (2.1 km, 2.7 km) and speed (3.5 km/s, 3.25 km/s). The high rupture velocity $\geq$90% v_S may be held primarily responsible for the strong directivity effect of this earthquake. We show that inversion of apparent source durations is intrinsically unable to resolve highly asymmetric bilateral ruptures, while inversion of full ASTFs misses part of the signal's complexity, suggesting the presence of deconvolution artifacts. We extend the analysis to the M_w 4.6 foreshock of the Lorca earthquake, inferring similar directivity parameters and slip pattern as for the mainshock. The rupture toward SW of both earthquakes suggests that this direction could be inherent to the fault segment.

1. Introduction

Extended fault inversions provide information on rupture size, rupture velocity, slip amplitude, or the configuration of main slip patches in an earthquake's rupture, among others. Rupture directivity is one of the most relevant aspects to emerge from such inversions, describing a potential asymmetry in rupture propagation outward from the hypocenter. Directivity is not arbitrary; it results from the initial and boundary conditions of the rupture. The distribution of stresses and friction on a fault, geometrical irregularities of the fault surface, or the difference of material properties between the fault bounding blocks may have an influence on the preferred direction of earthquake rupture propagation [e.g., *Boatwright and Cocco*, 1996; *Andrews and Harris*, 2005; *Ampuero and Ben-Zion*, 2008; *Brietzke et al.*, 2009; *Lengliné and Got*, 2011; *Kane et al.*, 2013]. In consequence, directivity might be an inherent property of rupture on certain faults or fault segments, and as such be predictable, at least in a statistical sense. On the other hand, directivity may have an important influence on ground motion. It may enhance significantly the peak velocity and peak acceleration in the direction of rupture propagation and increase damage in the forward direction because of focusing of seismic energy [e.g., *Boatwright and Boore*, 1982; *Miyake et al.*, 2001; *Somerville*, 2003]. Hence, rupture directivity is useful for understanding earthquake physics, the characteristics of a given fault system, or the possible asymmetry of patterns of earthquake losses and destruction. Last but not least, directivity effects provide strong evidence to resolve the fault plane ambiguity in point source focal mechanisms.

Predominantly unilateral rupture is a common characteristic of many large earthquakes [e.g., *McGuire et al.*, 2002] that can be analyzed from global records by evaluating relatively long period data. Rupture directivity is more difficult to assess for weak earthquakes. Different methodologies have been proposed to identify directivity [e.g., *Boore and Joyner*, 1978; *Somerville et al.*, 1997; *Warren and Shearer*, 2006; *Seekins and Boatwright*, 2010; *Caldeira et al.*, 2010; *Cesca et al.*, 2011], exploring for example the azimuthal patterns of peak

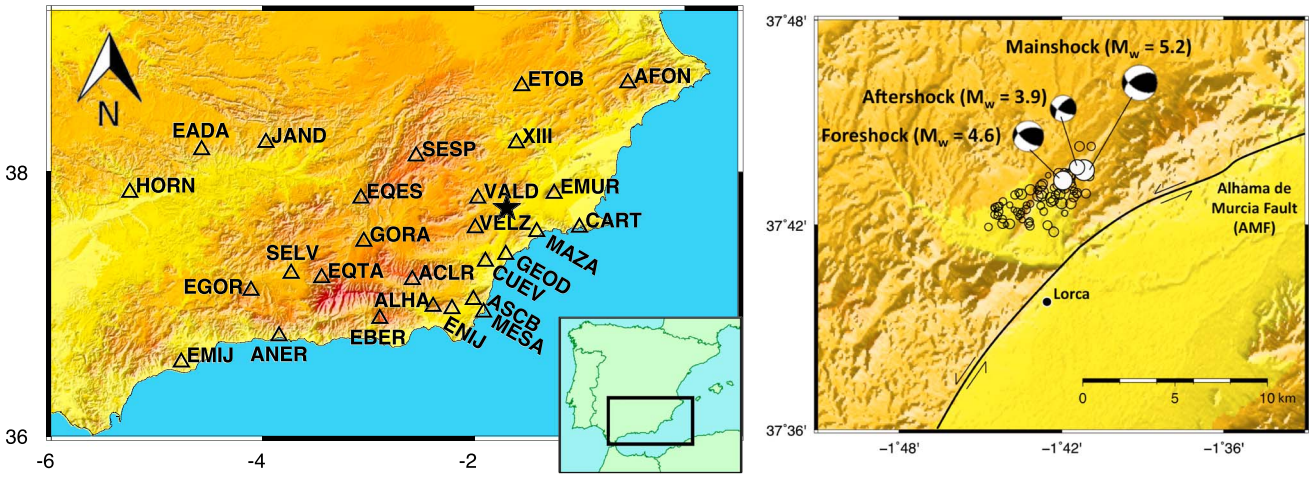

Figure 1. Recording geometry for the Lorca earthquakes (star) at near-regional broadband seismic stations (triangles). The close-up on the right shows relative locations and available moment tensor estimates for the earthquake sequence [*López-Comino et al.*, 2012].

ground velocity, acceleration, or apparent source duration. Apparent duration is predicted to be smaller in the forward direction of rupture propagation and larger in the backward direction [*Benioff*, 1955; *Ben-Menahem*, 1961], analogous to the Doppler shift in apparent frequency for a moving source. Apparent source durations for small earthquakes are typically inferred from empirical Green's function (EGF) analysis through the deconvolution of aftershock recordings from the waveforms [*Hartzell*, 1978]. The resulting apparent source time functions (ASTFs) are relative moment rate functions between the earthquake and the EGF, showing the history of moment release from the perspective of the observing station and through the phase velocity of the wave type under consideration. In practice, ASTFs will suffer from shortcomings of the chosen EGFs and numerical instabilities of deconvolution. In magnitude 5 earthquakes, rupture directivity translates into expected variations of apparent source duration of order of tenths of seconds [e.g., *López-Comino et al.*, 2012], which prompts concerns about the limits and reliability of such applications.

In this study, we reanalyze an event with recognized rupture directivity, the 11 May 2011, M_w 5.2 Lorca earthquake (Murcia, SE Spain, Figure 1), as well as its M_w 4.6 foreshock, which occurred almost 2 h before the mainshock. We estimate ASTFs for the earthquakes and analyze their performance in two fundamentally different inversion schemes, based on a 1-D and 2-D parameterization of the earthquake source, respectively. In particular, we try to estimate the uncertainties from either method. The 1-D parameterization assumes a line source [*Haskell*, 1964] in order to adjust the duration of ASTFs at different azimuths as a function of the rupture velocity, duration, and length, as well as the percentage and direction of slip asymmetry [e.g., *Caldeira et al.*, 2010; *Cesca et al.*, 2011; *Courboulex et al.*, 2013]. In the 2-D parameterization we invert the shape of ASTFs for the distribution of slip on a planar fault surface, and directivity will be expressed through the direction and separation between hypocenter and moment centroid [e.g., *Smith and Ekström*, 1997; *Weston et al.*, 2012]. Extended fault inversions are notorious for their nonuniqueness [e.g., *Olson and Apsel*, 1982; *Beresnev*, 2003; *Custódio et al.*, 2005; *Hartzell et al.*, 2007], and the description of uncertainties is an important problem. Basically, significantly different slip distributions may translate into fairly similar waveform predictions, giving rise to ambiguities and making inferences from a single best fitting model problematic. We apply a Popperian inversion strategy to the problem, generating a representative set of pseudorandom slip distributions, discarding falsified trial models on account of poor fit to the ASTFs, and treating all the remaining unfalsified models as our set of equivalent solutions to the inverse problem [*López-Comino et al.*, 2015]. We analyze the resolution of rupture directivity by calculating a directivity vector for each slip map of this solution set and compare with the uncertainties from line source inversions.

2. ASTFs for the Lorca Earthquakes

We exemplify the resolution of directivity effects with the 2011 Lorca earthquake sequence (Murcia, SE Spain, Figure 1). The mainshock at 16:47 on 11 May had a relatively modest magnitude of $M_w = 5.2$, yet it caused very

serious damage and nine fatalities in the city of Lorca. The disproportionally large impact of this event is certainly due to the proximity of Lorca to the epicenter and to the event's shallow depth (~5 km), but in addition, it may be a consequence of a pronounced rupture directivity [*López-Comino et al*., 2012; *Alguacil de la Blanca et al*., 2012]. These authors obtain an asymmetric bilateral rupture with 70% of the rupture propagation in SW direction (~N220°E), toward Lorca, and other authors suggest an even more unilateral rupture, also toward Lorca [*Santoyo*, 2013; *Rueda et al*., 2014; *Pro et al*., 2014]. Based on seismological and geological evidence, the Lorca sequence has been attributed to a major oblique reverse fault, the Alhama de Murcia fault (AMF) [*Martínez-Díaz*, 2002; *Masana et al*., 2004]. Faulting parameters for the mainshock (strike/dip/rake of N240° E, 54°, 44°) and M_w 4.6 foreshock (N247°E, 46°, 40°) coincide with the geometry of the fault. Another question of interest is whether available data are able to resolve the vertical component of rupture directivity, since updip propagation has been predicted for velocity-strengthening fault gouges at the outcrop of the AMF in the epicentral area [*Niemeijer and Vissers*, 2014]. To test the hypothesis that there might be a preferred direction of rupture propagation in the fault segment, we will extend our interest to the M_w 4.6 Lorca foreshock at 15:05 UTC 11 May, in order to compare possible similarities.

The M_w 4.6 and 5.2 Lorca earthquakes provide a useful example, given that directivity is accepted at least for the mainshock, and the sequence has been recorded at a dense network of near-regional seismic broadband stations in SE Spain (Figure 1). Despite the location of the earthquakes close to the southeastern margin of the Iberian Peninsula, the azimuthal coverage is fairly complete when combining the IAG (Instituto Andaluz de Geofísica) and IGN (Instituto Geográfico Nacional) permanent seismic networks, as well as the temporary INDALO deployment by IAG. Regional recordings of these shallow earthquakes show complex waveforms, and we recur to EGF deconvolution to isolate the signature of the source from the seismograms [*Hartzell*, 1978]. We approximate the impulsive response of the Earth through recorded waveforms of the largest aftershock (M_w 3.9) as EGFs. This aftershock has very similar focal mechanism and source depth as the M_w 4.6 foreshock and 5.2 mainshock we want to address [*López-Comino et al*., 2012]. We obtain ASTFs between the target waveforms and our EGFs at regional stations out to 250 km distance, applying deconvolution to *P* wave windows (length equal to the *S*-*P* time) and *S* wave windows (length 15–20 s). Two different deconvolution methods are tested and compared. First, frequency domain deconvolution through spectral division is applied. To stabilize deconvolution, we introduce a Gaussian filter-width factor of 10 (this parameter corresponds to a time domain pulse with approximate width of ~0.5 s) and water level of 0.01 [*López-Comino et al*., 2012]. Second, time domain deconvolution is applied to the same waveforms, using an iterative approach that constructs the deconvolved function as a sequence of Gaussian pulses with adjusted amplitudes and time lags [*Ligorría and Ammon*, 1999; *Kikuchi and Kanamori*, 1982]. Amplitudes and lag times are obtained through cross correlation between the EGF and the target waveforms. In each iteration, a Gaussian pulse is added to the deconvolved function and its prediction is subtracted from the target waveforms, until we truncate deconvolution after 200 iterations. We choose the same pulse width as for the Gaussian filter in frequency domain deconvolution. Figures S1 and S2 in the supporting information show the details of the deconvolution process in the frequency and time domain, respectively, and the calculated ASTFs for some example stations.

The obtained ASTFs show plausible source time histories, with a well-defined signal clearly distinguishable from the background level (Figure 2). Frequency and time domain results are very similar, except for the causal signal of the latter, imposed by construction of the time domain deconvolution procedure. A manual picking is performed to estimate the apparent durations of the ASTFs, taking as reference points the intersection of the initial and final slopes of the time functions with the baseline. Technically, the picking errors may be supposed to be about 0.05 s; however, the different characteristics of oscillatory and asymptotic waveforms may translate to larger uncertainties in some stations. For the mainshock, we infer apparent durations of 0.45–1.05 s from *P* waves and 0.75–1.4 s from *S* waves [*López-Comino et al*., 2012]. Note that we obtain the same values of apparent durations with both deconvolution techniques. Most ASTFs show a simple shape of the time functions with one single source pulse. Exceptions are the longest ASTFs obtained for the mainshock recorded at NE azimuth, which show a sequence of two or three overlapping pulses. These structured ASTFs may be linked to heterogeneous moment release with two or three slip patches for the mainshock. However, this is at odds with reported geodetic and seismological fault models for the Lorca mainshock, showing a smooth and continuous distribution of slip [*Martínez-Díaz et al*., 2012; *De Michele et al*., 2013; *Santoyo*, 2013; *Rueda et al*., 2014; *Pro et al*., 2014]. As exception, *González et al*. [2012] proposes a separate

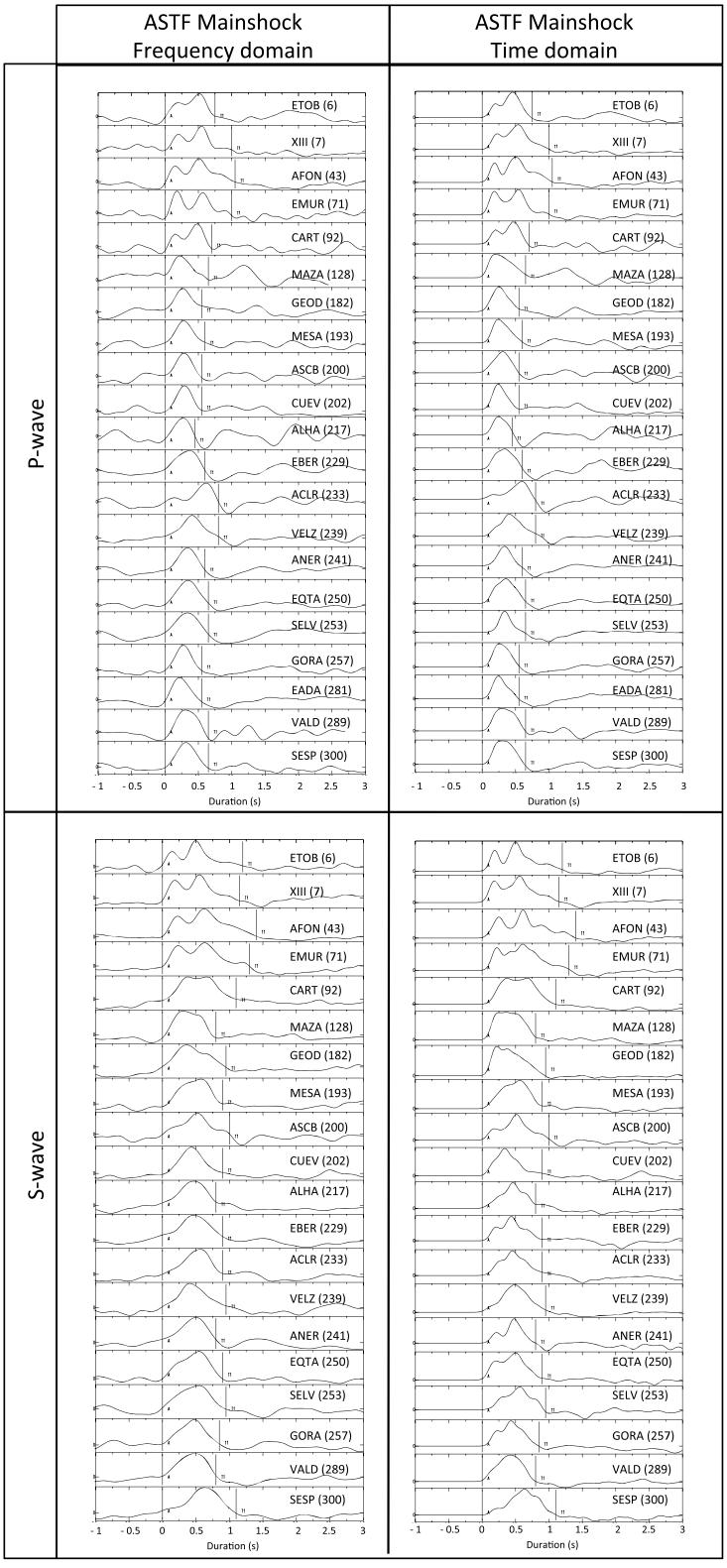

Figure 2. Apparent source time functions (ASTFs) for the Lorca M_w 5.2 mainshock. Deconvolved functions from *P* and *S* waves are shown, as well as the results from different deconvolution schemes ((left column) frequency deconvolution; (right column) time domain deconvolution). ASTFs are plotted in station's azimuthal order, showing a systematic variability of apparent source durations (the duration's measurements are indicated on the traces and in Table S1). Labels indicate the station name and the azimuth for each ASTF.

Table 1. Inversion of Apparent Durations for the Lorca M_w 5.2 Mainshock Using a Trust-Region Algorithm and a Grid Search[a]

	Trust-Region Algorithm	Grid Search
Directivity (deg)	213 ± 12	224 [174, 268]
Bilateral percentage (%)	67 ± 4	60 [50, 78]
Rupture velocity (km/s)	3.50 ± 1.81	3.25 [2.0, 3.5]
Rupture length (km)	2.1 ± 0.7	3.0 [1.0, 3.6]
Total rupture time (s)	1.0 ± 0.1	0.75 [0.56, 0.96]
Rise time (s)	0.4	0.2 [0.2. 0.6]

[a]The best fitting value and their uncertainties are shown for each involved parameter. Uncertainties using a grid search are shown with an interval in brackets according to a L1 threshold value for the acceptable solutions.

secondary patch with minor slip near the surface. We will address potential heterogeneity of fault slip in section 4. Apparent durations for the foreshock are 0.35 to 0.8 s for *P* waves and 0.6–1.2 s for *S* waves (Figure S3).

3. Line Source Directivity Analysis

In this section, we use the inferred apparent source durations of the deconvolved ASTFs to estimate source parameters associated to a line source [*Haskell*, 1964]. Durations for the Lorca mainshock show smooth azimuthal variability characteristic of rupture directivity [*Benioff*, 1955; *Ben-Menahem*, 1961]. Duration measurements are larger to the NE and shorter to the SW, associating these directions with the backward and forward directions of predominant rupture propagation, respectively. To quantify directivity, we compare the azimuthal pattern of apparent durations to the theoretical patterns for unilateral and (asymmetric) bilateral rupture using the parameterization of *Cesca et al*. [2011]. For unilateral rupture, duration as a function of azimuth $\tau(\phi)$ can be written as

$$\tau(\phi)_{\mathrm{UNI}} = t_r + \frac{L}{v_R} - \frac{L}{v_{P,S}}\cos(\phi - \alpha) \tag{1}$$

Parameters in this model are the rupture length L, the constant rupture velocity v_R, the *P* and *S* wave velocities ($v_{P,S}$), respectively, the azimuth of rupture directivity α, and the rise time t_r. The first two terms, $t_r + L/v_R$, are the total rupture time, and we may expect significant trade-offs between the involved parameters. Equation (1) assumes horizontal wave propagation from the source to the receiver, i.e., takeoff angles $\Psi = 90°$ (compare, e.g., with *Courboulex et al*. [2013]). This choice is supposed to represent the bulk behavior of the wavefield for shallow earthquakes at regional distances, even though individual components of the wavefield will leave the source at angles $\Psi \neq 90°$, in general. For a bilateral line source with general asymmetry, the apparent durations are given by

$$\tau(\phi)_{\mathrm{BI}} = \max[t_r + (1-\chi)]\left(\frac{L}{v_R} - \frac{L}{v_{P,S}}\cos(\phi - \alpha)\right), \quad t_r + \chi\left(\frac{L}{v_R} - \frac{L}{v_{P,S}}\cos(\phi - \alpha)\right) \tag{2}$$

The asymmetry χ is defined between 0 (unilateral rupture, equation (1)) and 0.5 (symmetric bilateral rupture); that is, the first argument of the max function corresponds to the long leg of rupture propagation. We explore two different strategies for estimating line source parameters. First, following *López-Comino et al*. [2012], we invert directly the nonlinear functions (equations (1) and (2)) for duration, fault length, ands the azimuth and percentage of rupture directivity applying a search algorithm in Matlab (lsqcurvefit, nlparci). Minimization is achieved through a trust-region algorithm based on the reflective Newton method [*Coleman and Li*, 1994, 1996]. We invert the total duration as an additional composite source parameter with more direct expression in observed durations and less susceptibility to trade-offs, resulting in smaller errors. In order to reduce trade-offs, we assume a fixed rise time. *P* and *S* wave velocities are chosen as 5.4 km/s and 3.5 km/s, respectively, which are appropriate for the region studied [*Martínez Díaz*, 1998]. Parameter errors are approximated from the residuals using the Jacobian of partial derivatives of the function on each point as sensitivity matrix. We report 95% confidence intervals for individual parameters (Table 1). Additionally, we solve the nonlinear inverse problem through a full grid search for the involved parameters, including the rise time in reasonable intervals and increments (α in [N0°E–N360°E], L in [1 km–5 km], v_R in [2.0 km/s–3.5 km/s], t_r in [0.2 s–1.0 s], and χ in [0.0–0.5]). Model performance is evaluated through the L1 misfit to *P* and *S* wave apparent durations at all stations, which are inverted simultaneously. Besides being an alternative way to adjust a line source model to observed durations, the grid search permits an independent assessment of parameter errors, since L1 misfit for all trial models (~4.4 million models) is available and we can directly identify all solutions with similar misfit.

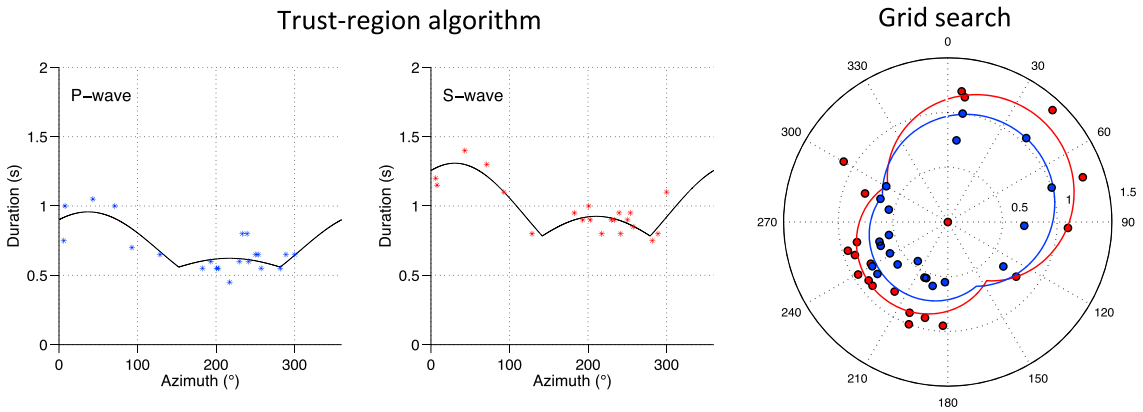

Figure 3. Inversion of apparent durations for the Lorca M_w 5.2 mainshock using a trust-region algorithm and grid search, respectively. First and second columns show *P* wave measurements (blue) and *S* wave measurements (red) along with synthetic predictions for the inverted model. The last column shows fits from L1 norm grid search for *P* and *S* wave measurements jointly in a polar plot (radial axis apparent source duration, blue for *P* wave, red for *S* wave).

The best fits for the Lorca mainshock correspond to asymmetric bilateral ruptures (Table 1). These solutions reproduce the two-lobe azimuthal patterns observed in the apparent duration (Figure 3), where the principal and secondary maxima correspond to the backward directions for the long and short leg of rupture propagation according to equation (2). From full grid search, we infer a repartition of rupture in either direction of about 60:40, while the trust-region algorithm yields 67:33. The net directivity is estimated as being N224°E and N213°E, respectively, in agreement with rupture along the NW dipping nodal plane of the mechanism and previous directivity analyses. Other line source parameters are also similar from both inversion approaches (Table 1), yielding reasonable estimates for a M_w 5.2 earthquake. Both methods suggest high rupture speed (3.25 km/s and 3.5 km/s, respectively), approximating the *S* wave speed (3.5 km/s), although uncertainties are large for this parameter because of trade-offs with rupture length (3.0 km and 2.1 km, respectively) and rise time (0.2 s and 0.4 s, respectively). While reported errors for the trust-region algorithm are obtained from the Jacobian (see above), errors for grid search inversion are defined through a L1 threshold value for acceptable solutions. We consider acceptable solutions with L1 misfit measures between the global minimum (0.10 s) and the minimum plus 0.05 s, which represents plausible picking errors. Comparison of errors derived from the trust-region algorithm and grid search, respectively (Table 1), suggests that the L1 threshold of 0.15 s may be a conservative choice. In both cases, the direction of rupture directivity and the partitioning on the short and long legs of the asymmetric line source can be considered well resolved. Other parameters remain unconstrained from the inversion: uncertainties of rupture velocity and length are of the same order as the parameter estimates, large parameter errors go along with significant residuals of apparent durations, and residuals are greater than plausible picking errors on many individual ASTFs. In particular, a 1-D line source model for the foreshock reveals limitations and clear inconsistencies such as the length estimates for the mainshock being smaller than for the foreshock (Figure S4 and Table S2), which suggests additional measurement errors related to deconvolution instability and inaccuracy of the EGFs.

Despite the moderate asymmetry of our best fitting model, we recall that purely unilateral rupture (equation (1)) still provides a reasonable fit to apparent durations for the Lorca mainshock, at least for *P* waves [*López-Comino et al.*, 2012]. This behavior can be understood through the parameterization of the problem. Formally, asymmetric bilateral rupture (equation (2)) is the most general representation, incorporating the repartition of rupture into opposite directions as an additional free parameter and including a purely unilateral rupture as a special case with $\chi = 0$. However, there exists a significant null space. For highly asymmetric ruptures, the short leg term inside the max function is the smallest term at all azimuths, does not leave any signature in apparent source durations, and cannot be resolved from this kind of observations. The threshold on χ for the disappearance of the short leg term depends on rupture speed:

$$2\chi \leq 1 - \frac{v_R}{v_{P,S}} \rightarrow \tau(\phi)_{\mathrm{BI}} = t_r + \frac{L'}{v_R} - \frac{L'}{v_{P,S}}\cos(\phi - \alpha);\ L' = (1-\chi)L \tag{3}$$

Equation (3) shows that for small χ, equation (2) degenerates into a unilateral rupture with underestimated rupture length (equation (1)). For typical relations between *P*, *S*, and rupture velocity ($v_R = 0.8v_S$ and

$v_P = 1.73 v_S$), this criterion corresponds to $\chi = 0.27$ for *P* waves, and $\chi = 0.1$ for *S* waves. There is no formal sensitivity to larger asymmetries, and the problem may be aggravated by measurement errors. For the Lorca mainshock, inverted asymmetry is near the resolution limit for *P* waves, but well resolved by *S* waves, which is confirmed by the clear secondary maxima in the azimuthal pattern of apparent *S* wave durations. To handle the general case of arbitrarily asymmetric ruptures, we must take into account the full time history of ASTFs instead of durations only.

4. Extended Fault Inversion Through Falsification

Extended fault inversion adopts a 2-D parameterization of the source model and assigns locally variable slip values in a regular mesh of subfaults. This treatment takes into account the shape of the ASTFs, which will be modeled as the sum of subfault contributions. We assume a planar faulting geometry and orientate the model to the point source faulting parameters inferred from moment tensor inversion [*López-Comino et al*., 2012]. We assume propagation effects to be fully contained in the EGF waveforms and model ASTFs for *P* and *S* waves directly by the superposition of time-lagged elementary slip velocity functions from a total number of n discretized subfaults:

$$\mathrm{ASTF}_{i,P/S}(t) = \sum_{j=1}^{n} a_j S\left(t - \Delta t_{ij}\right); \quad \Delta t_{ij} = \frac{|\xi_j|}{v_R} - \frac{\xi_j \cdot \gamma_i}{v_{P/S}} \tag{4}$$

Here *i* and *j* are indices of the respective recording stations and subfaults. We discretize the mainshock fault model into 17×17 square subfaults with size of 0.3 km, and the aftershock into 13×13 subfaults with size of 0.25 km, with ξ_j being the subfault position vectors from the hypocenter centered of the fault plane. This corresponds to 5.1 km and 3.25 km long fault models, which exceed the rupture lengths plus 95% confidence errors obtained from line source inversion in order to allow for distributed slip patterns. The elementary slip function *S* is chosen by trial and error as a triangle with rise times of 0.1 s for *P* waves in both events and 0.2 s and 0.15 s for *S* waves for the mainshock and foreshock, respectively. Delay times Δt_{ij} are assigned analogous to equation (1), taking into account contributions from rupture propagation and source-receiver geometry. We parameterize a single, outward propagating rupture with constant rupture speed v_R. Takeoff vectors γ_i assume horizontal wave propagation like for the line source parameterization, as well as parallel rays, because distances on the fault plane are small compared to the source-receiver distances. ASTF waveforms are normalized to unit area prior to inversion in order to compensate potential differences in the underlying radiation patterns for EGFs and the target earthquakes. Slip amplitudes a_j are scaled to physical quantities by constraining the sum of subfault scalar seismic moments to be equal to the scalar moment of the earthquake from point source inversion. We assume a standard crustal rigidity of 30 GPa for this conversion.

Equation (4) represents an overdetermined linear system common in extended source inversion, which could be solved through matrix inversion, using the typical stabilizing constraints to mitigate the nonuniqueness of the problem [e.g., *Olson and Apsel*, 1982; *Hartzell and Heaton*, 1983]. In order to keep track of potential ambiguities of the inversion, we use a search technique instead. This involves the generation of a representative set of slip distributions a_j and systematic comparison of the corresponding forward predictions to the target ASTFs obtained from EGF analysis. We evaluate the model search through a Popperian strategy, rejecting as falsified those trial models that do not produce acceptable fits. The surviving, unfalsified models constitute our set of possible solutions to the inverse problem. Here we summarize briefly the inversion sequence and refer to *López-Comino et al*. [2015] for a detailed description. We generate source models through spectral synthesis for pseudorandom phase and 2-D von Karman distribution of slip heterogeneity on the fault [*Mai and Beroza*, 2002], followed by an appropriate postprocessing in order to impose the positivity of slip and the limit of earthquake rupture. We introduce 10,000 trial slip distributions into the model search. This number is justified by a control test, showing the general repetition of similar source models (normalized cross correlation > 0.9) among an inventory of 10,000 models [*López-Comino et al*., 2015]. To evaluate the model performance, we choose a normalized L1-fit of the residuals as objective function (equation (5)). Compared to higher order Minkowski distances like the L2-norm, L1 is more sensitive to small amplitudes and rewards an appropriate fit to the tails of ASTFs.

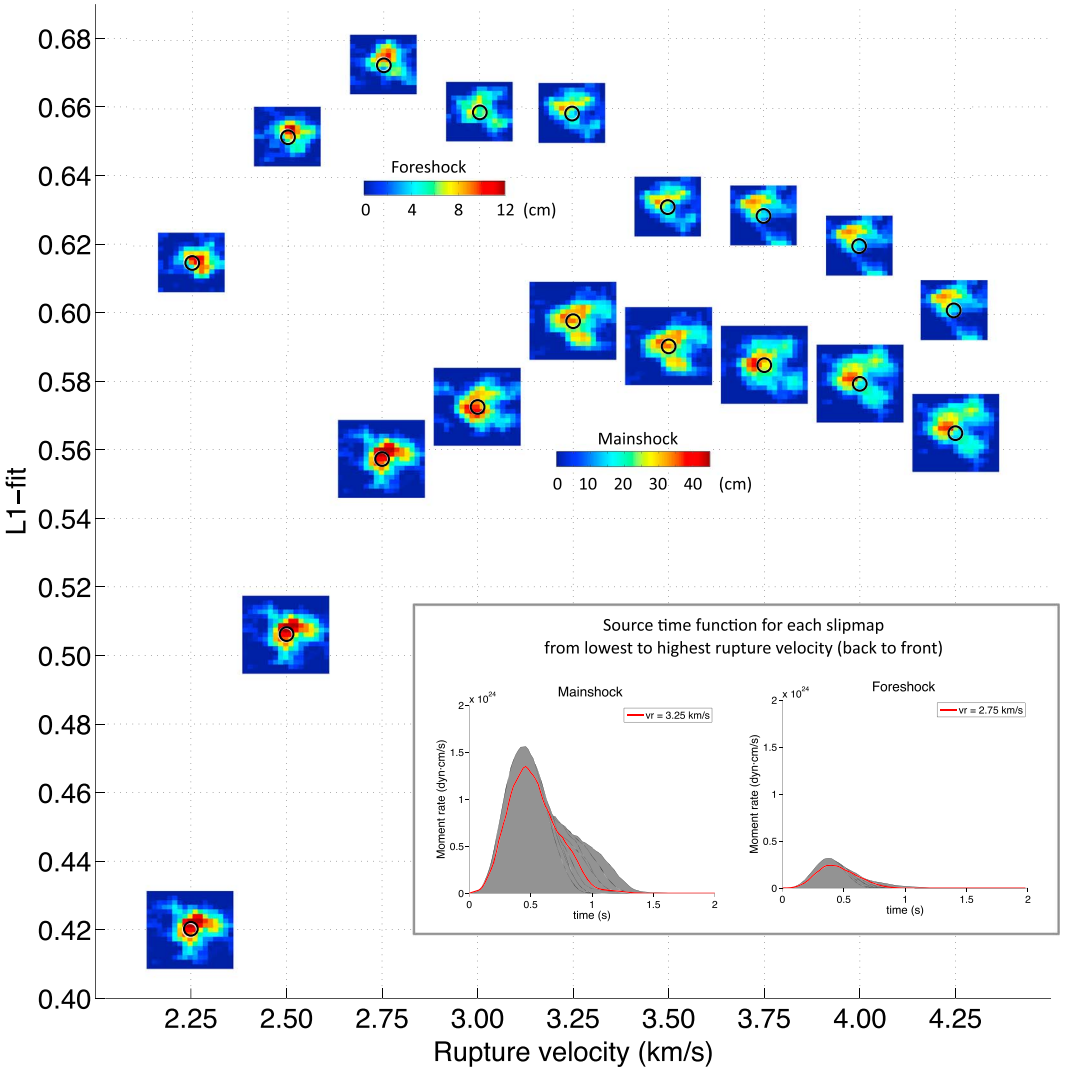

Figure 4. Extended fault inversion for the Lorca mainshock and foreshock using different values of rupture speed. We show the formally best fitting model at each trial speed using normalized L1-fit as objective function. The black open circles mark the L1-fit and the hypocenter of each slip map. L1-fits are larger in foreshock inversions compared to the mainshock, due to the simpler shape of the ASTFs. The preferred rupture speed is higher for the mainshock. Slip amplitudes are given in cm (color bar). The inset shows the corresponding source time functions, showing the expected trade-off between duration and rupture speed. The red lines mark the source time functions for the best fitting models.

This gives emphasis on apparent source durations in the data domain, as well as to the limits of rupture in the model domain.

$$L1 = 1 - \sum_i |\mathrm{obs}_i - \mathrm{pre}_i| / \sum_i |\mathrm{obs}_i| \quad (5)$$

Inversion is prepared by testing trial values for rupture speed from 2.25 km/s to 4.25 km/s (Figure 4). We select the preferred rupture speed according to normalized L1-fit of the formally best fitting model, setting this value for subsequent Popperian analysis. The L1-fit versus v_R curves are smooth with clear maxima, indicating rupture speed of 3.25 km/s for the mainshock and 2.75 km/s for the foreshock. Rupture speeds are slightly lower than those obtained from line source inversion, but remarkably similar within the large uncertainties of line source rupture speed (Table 1). In case of 2-D inversion, we obtain very similar L1-fits for models within ±0.5 km/s with regard the best rupture speed (Figures 4 and 5). Beyond that limit, slip distributions vary significantly, illustrating the potential bias of unresolved rupture speed. Generally, source time functions shorten as we increase the rupture speed (inset in Figure 4), while slip becomes more distributed over the fault model.

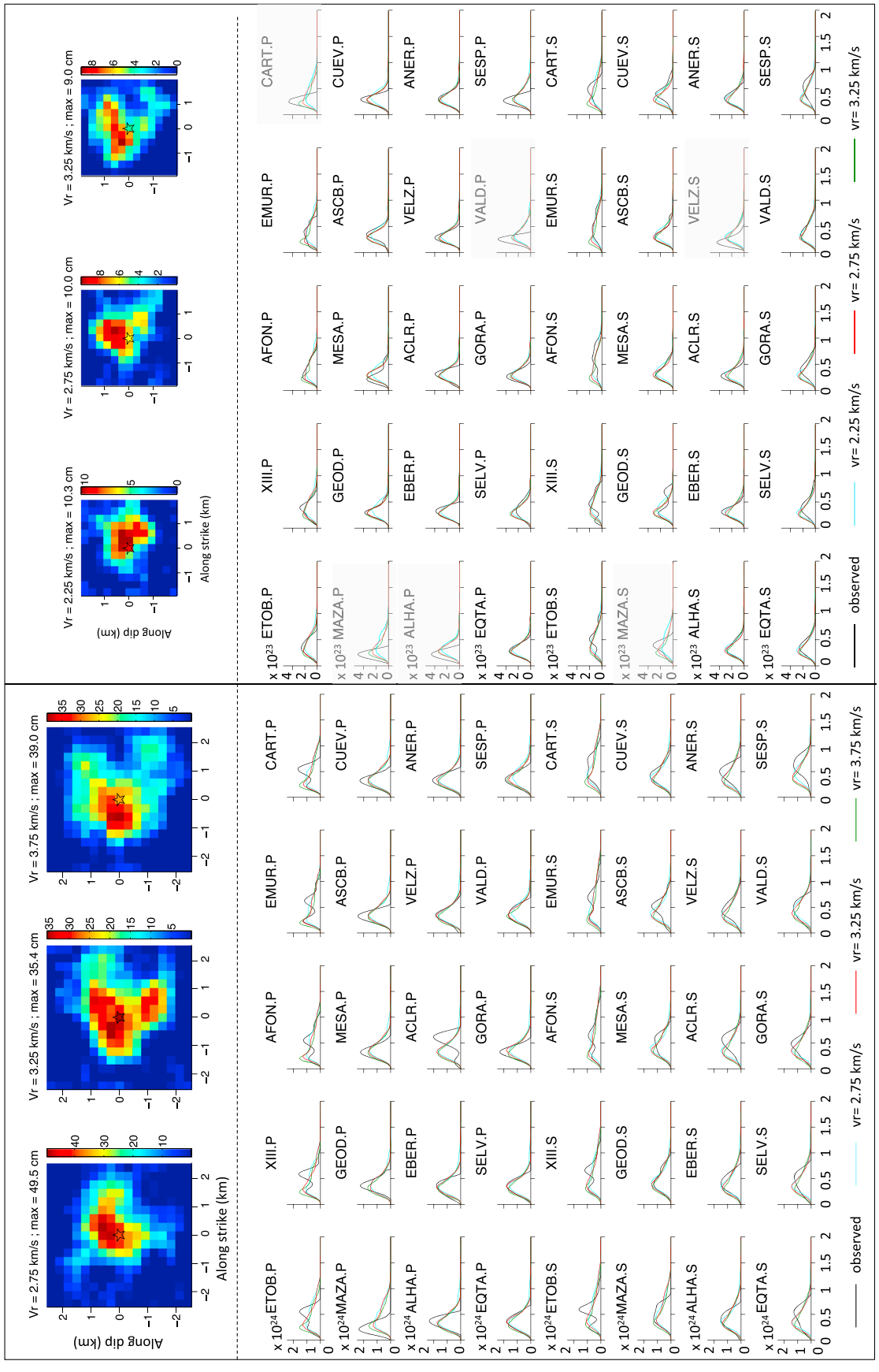

Figure 5. Slip maps and synthetic predictions corresponding to observed ASTFs (black lines) for the formally best fitting models ((left) mainshock and (right) foreshock). We compare results for the formally best fitting tested rupture speed (central slip maps, red lines for synthetic ASTFs), a lower rupture speed (−0.5 km/s, left maps, cyan lines) and higher rupture speed (+0.5 km/s, right maps, green lines). ASTFs excluded from the foreshock inversion (weight zero) are shown with transparency. Color bars of each slip map are in centimeters. Vertical axis for ASTFs is in dyn cm/s and horizontal axis is in seconds.

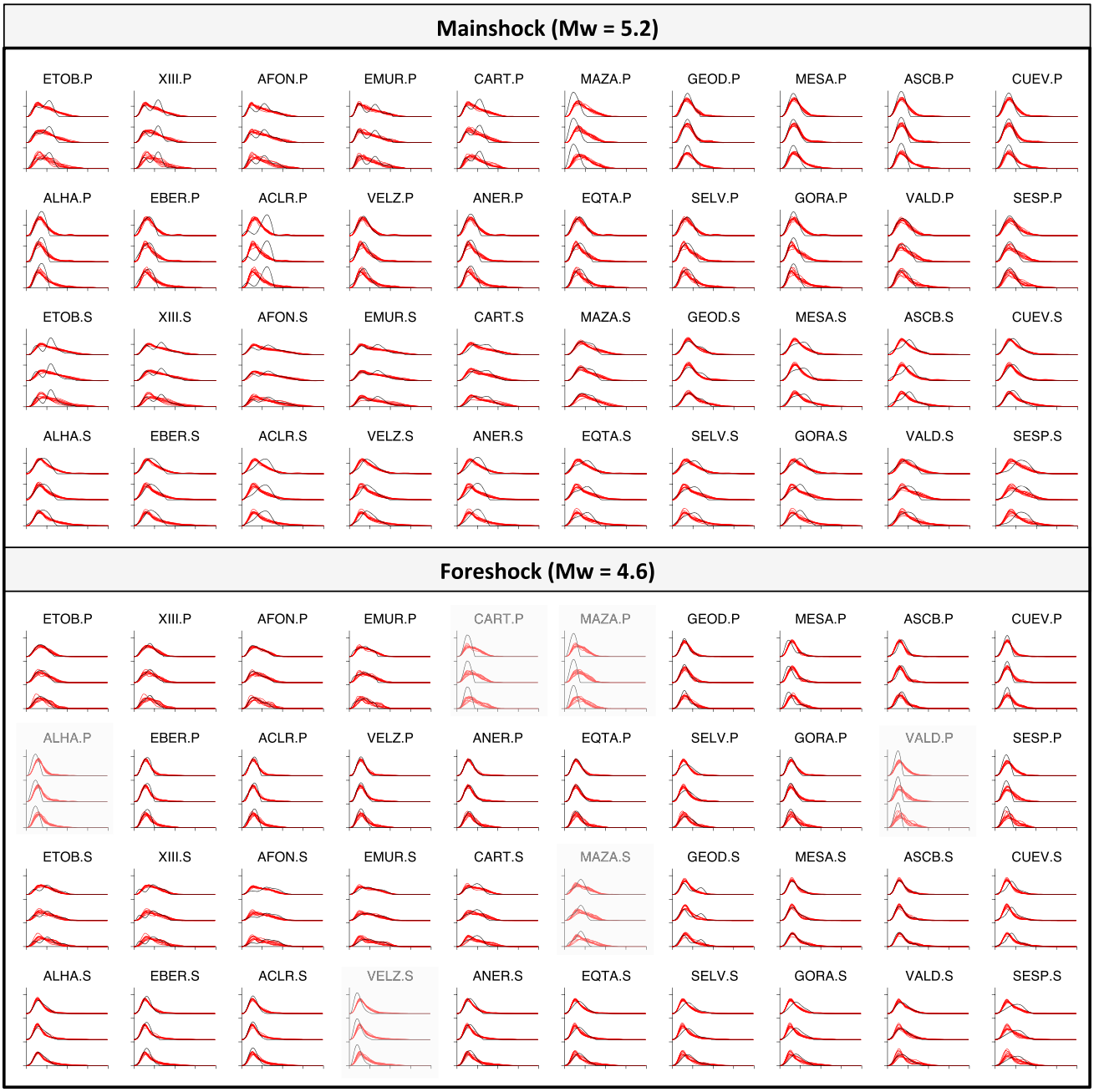

Figure 6. Comparison of waveform matches for models with different L1-fit values for the (top) mainshock and the (bottom) foreshock. For each station and wave type (*P* or *S*), we show the observed ASTF (black line) and three levels of data fit (red lines): the 10 best models (first level), 10 models with L1-fits that fall within 5% of the best fitting model (second level), and 10 models with L1-fits that fall within 10% of the best fitting model (third level). The transparency and time scale are as in Figure 5.

This corresponds to the analogous trade-off between fault length and rupture speed in line source inversion. The shape of the ASTFs is recovered reasonably well with these slip models (Figure 5). Exceptions are on the one hand some individual waveforms (e.g., mainshock at MAZA, ACLR) that may reflect local effects since ASTFs at neighboring stations are reproduced well. On the other hand, no slip distribution is able to fit the two or three pulses observed at stations located NE of the epicenter, which indicates possible stability problems with these ASTFs (see discussion section). Several poor fits for the foreshock led to the exclusion of these waveforms from computing the total L1-fit.

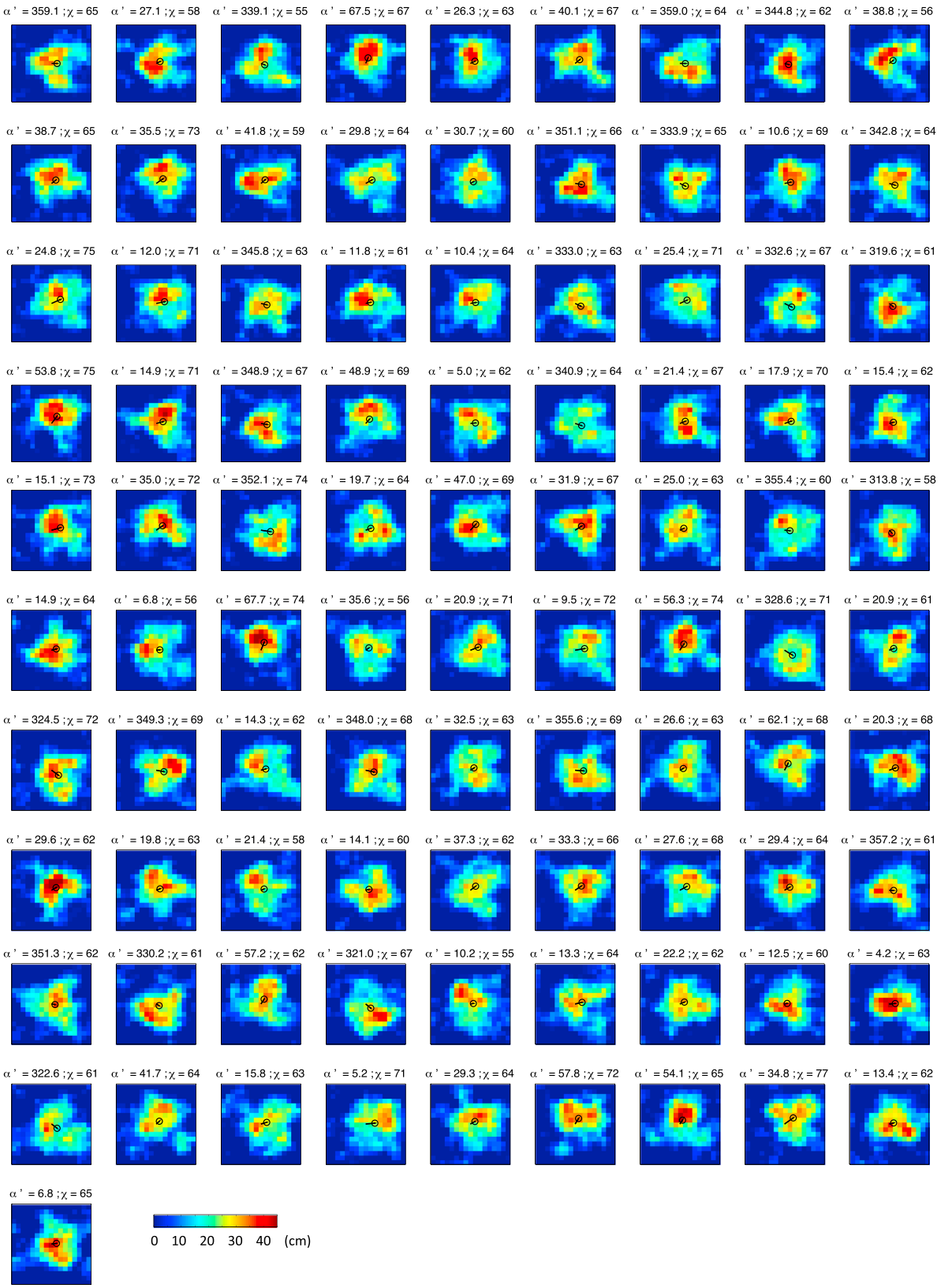

Figure 7. Solution ensemble from Popperian inversion for the mainshock, consisting of 91 unfalsified trial models with L1-fit ≥ 0.5475. Slip maps are sorted according to L1-fit in descending order. For each slip map we show the directivity vector from the hypocenter to the moment centroid (black open circle). Angle of the directivity vector in the rupture plane (α') in degrees and the asymmetry of rupture (χ) in percentage are labeled on top of the slip maps.

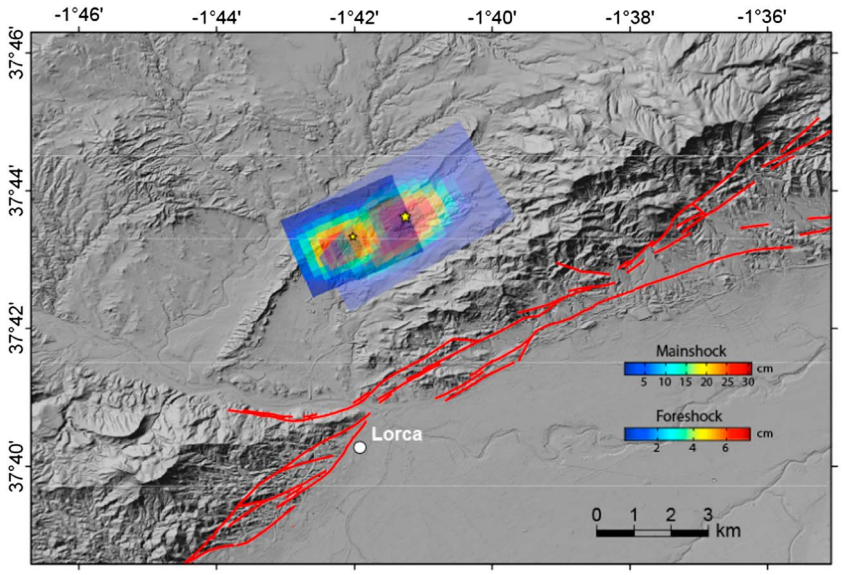

Figure 8. Average slip models for mainshock and foreshock projected onto a map of the epicentral area. The Lorca city center and the surface trace of the Alhama de Murcia fault are also shown [*Martínez-Díaz et al*., 2012].

Popperian inversion is motivated by the idea that best fitting models like in Figures 4 and 5 are a rather incidental choice among a number of possibilities, all of them leading to roughly equivalent fit. We should preferably invert for an ensemble of acceptable models and analyze their fluctuations to retrieve stable conclusions [*López-Comino et al*., 2015]. The size of this solution set depends on the misfit criterion and threshold that separates falsified models from acceptable models. We establish this limit by visual inspection of waveform matches. Figure 6 compares the fits of the 10 formally best models to selected inferior models. Their normalized L1-fits are about 0.05 and 0.1 lower than the best fitting solution. Owing to the low complexity of the target ASTFs, the general level of fit is good, but significant mismatch appears for the models with the lowest scores. Clear discrepancies at the tail of the ASTFs (e.g., *P* waves in CUEV for both events) indicate that those models can be considered falsified on account of wrong predictions of duration. Assuming the best L1-fit minus 0.05 as threshold, 91 and 193 slip distributions are retained for the mainshock (Figure 7) and the foreshock (Figure S5), respectively. These solution sets are heterogeneous considering many details such as the position and amplitude of peak slip: individual, coequal models will lead to different interpretations. On the other hand, models coincide on the fundamental pattern of a single, compact slipping area around the hypocenter, with this consensus being transmitted to the average slip maps computed from our solution sets (Figure 8). The average slip map for the mainshock is in qualitative agreement with line source directivity analysis, showing asymmetric slip centered SW of the hypocenter. The slip map for the foreshock reveals a similar asymmetry. Peak slips are about 31 cm and 7 cm, respectively. Individual solutions, however, feature diverse peak slip values of 30–50 cm and 7–12 cm, respectively. Averaging the different distributions leads to slip estimates near the lower bound of amplitude fluctuations due to a lack of alignment of high-slip patches in individual solutions.

5. The Resolution of Directivity

Individual models in the solution set show different fine structure of slip, which translates into variable directivity of rupture propagation. The average slip maps (Figure 8) are in general not representative of the directivity of individual models. Based on the premise that all unfalsified models are equally valid, we may evaluate the resolution of the directivity parameters. In the seismological literature, the interpretation of directivity from slip maps is usually accomplished through qualitative statements, which, for example, refer to the bulk asymmetry in slip distributions with respect to the cardinal points or classify patterns into updip and downdip. Here we condense rupture directivity into two objective parameters, direction and amount of asymmetry, like in line source inversion. Direction is inferred from the vector between hypocenter and moment centroid of the slip distribution (see Figure 7). It is expressed through the angle α' of the directivity vector

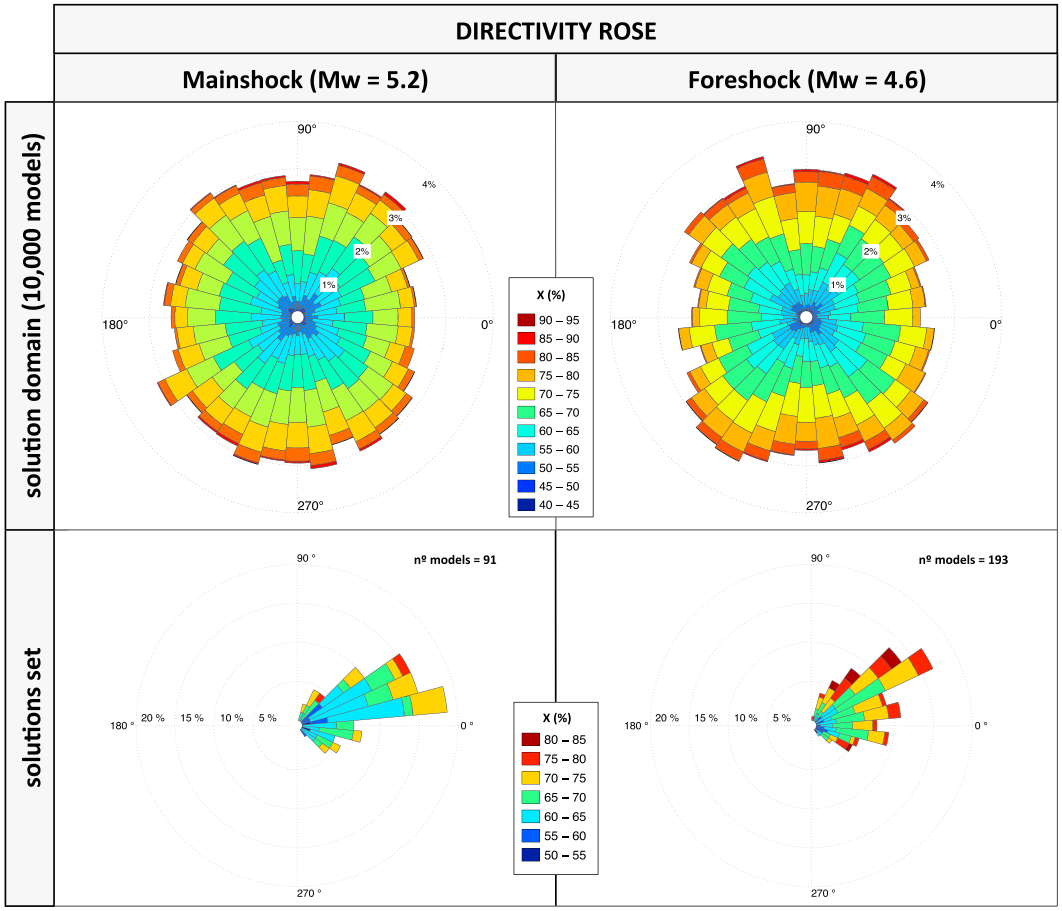

Figure 9. Directivity rose for (top row) tested trial models and (bottom row) solution sets from Popperian inversion. Results are shown for the (left column) mainshock and the (right column) foreshock. Angle of the directivity vector in the rupture plane (α') and the asymmetry of rupture (χ) (color bar) are identified for each set of slip maps. Concentric circles mark the percentage with respect to all slip maps considered in each directivity rose (the label on the right corner of each bottom box shows the total number of models).

in the rupture plane (defined analogous to the rake angle in faulting mechanisms) or the angle α of the projection of this vector onto a horizontal plane (analogous to strike, clockwise from north, as in line source inversion). The asymmetry of rupture is again given by the ratio χ of fault slip in forward and backward direction from the hypocenter; subfault slip adds to the forward/backward fraction if the scalar product between subfault position vector, and directivity vector is positive/negative. All vectors are shown in Figures 7 and S2 (see labels α' and χ) and can be analyzed jointly in a single graph that we call a "directivity rose" (Figure 9).

The rose diagram for directivity is a polar representation of directivity angle α' and the relative frequency of occurrence among the data set. Additionally, color bands in each spoke represent different amounts of asymmetry χ. The directivity rose for the entire set of 10,000 trial solutions confirms a rather uniform prior distribution of tested directivity angles, except for the oval outline produced by the slightly different correlation lengths assumed along strike and along dip according to the scaling relations in *Mai and Beroza* [2002]. The percentage of asymmetry is distributed relatively uniformly for small values (50%–75%), but there is a lower probability to obtain highly asymmetric slip maps (≥80%) from pseudorandom phase values. Note that sporadic values of $\chi < 50\%$ in Figure 9 are artifacts from the projection of discretized subfault displacements. Just as values for χ between 50% and 60%, they correspond to essentially symmetric distributions. Models with asymmetry larger than 80% could be labeled in a qualitatively way as unilateral rupture (examples in Figure 7). The directivity rose for the solution sets (Figure 9, bottom row) show a confined distribution of viable values for α', constrained to angles within approximately ±45° from the directivity of the formally best fitting models. There are no secondary maxima in the distribution, which means no fundamental ambiguities

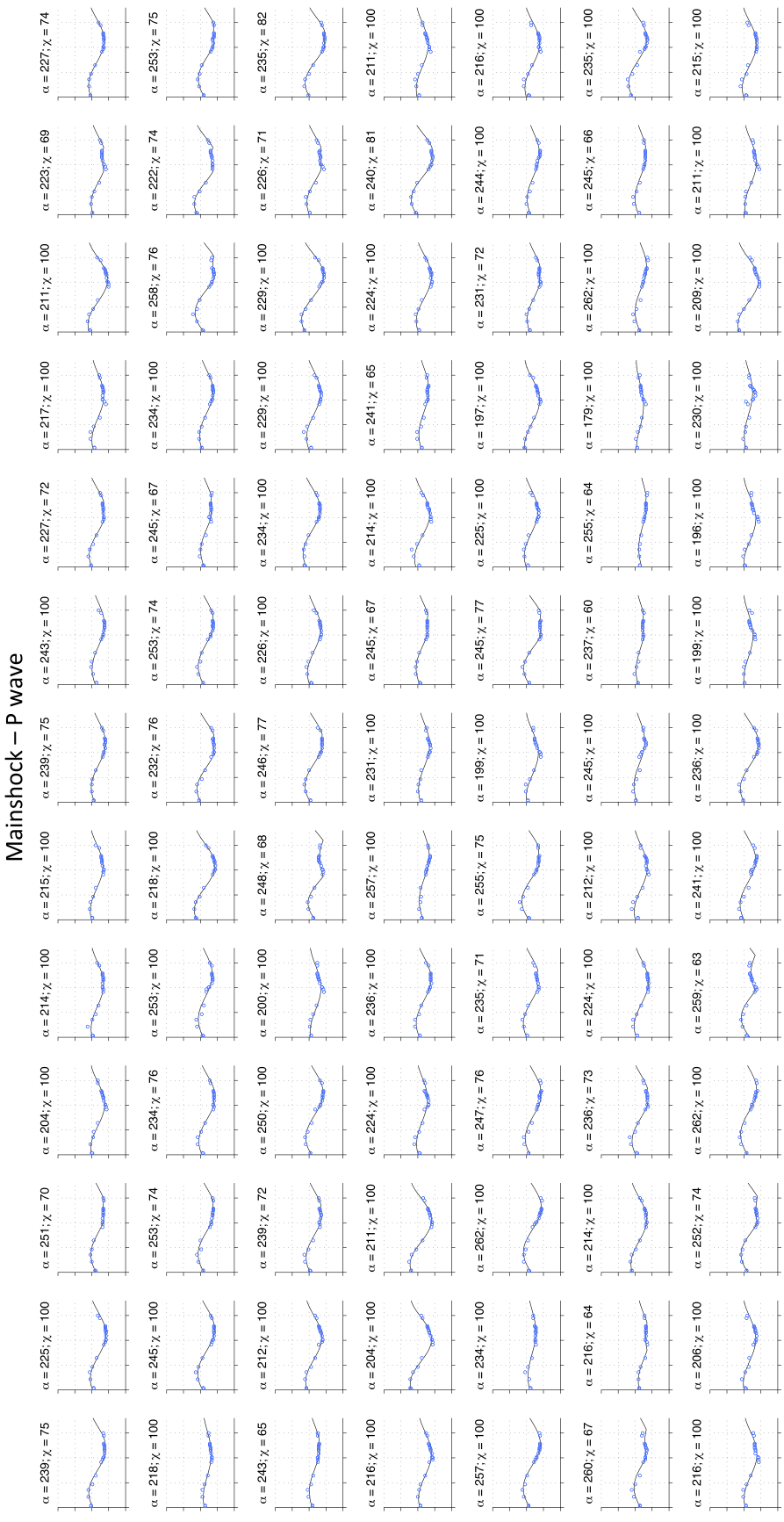

Figure 10. (a) Line source analysis for the synthetic ASTFs durations from the solution set of the mainshock for *P* wave. We show the synthetic apparent duration for each station (open blue circles) and the best curve fit (black line) considering unilateral or bilateral rupture (equations (1) and (2)) for each individual solution from the ensemble. The azimuth of rupture directivity (α) in degrees and the asymmetry of rupture (χ) in percentage are labeled on top of each curve fit. Axes scale as in Figure 3.

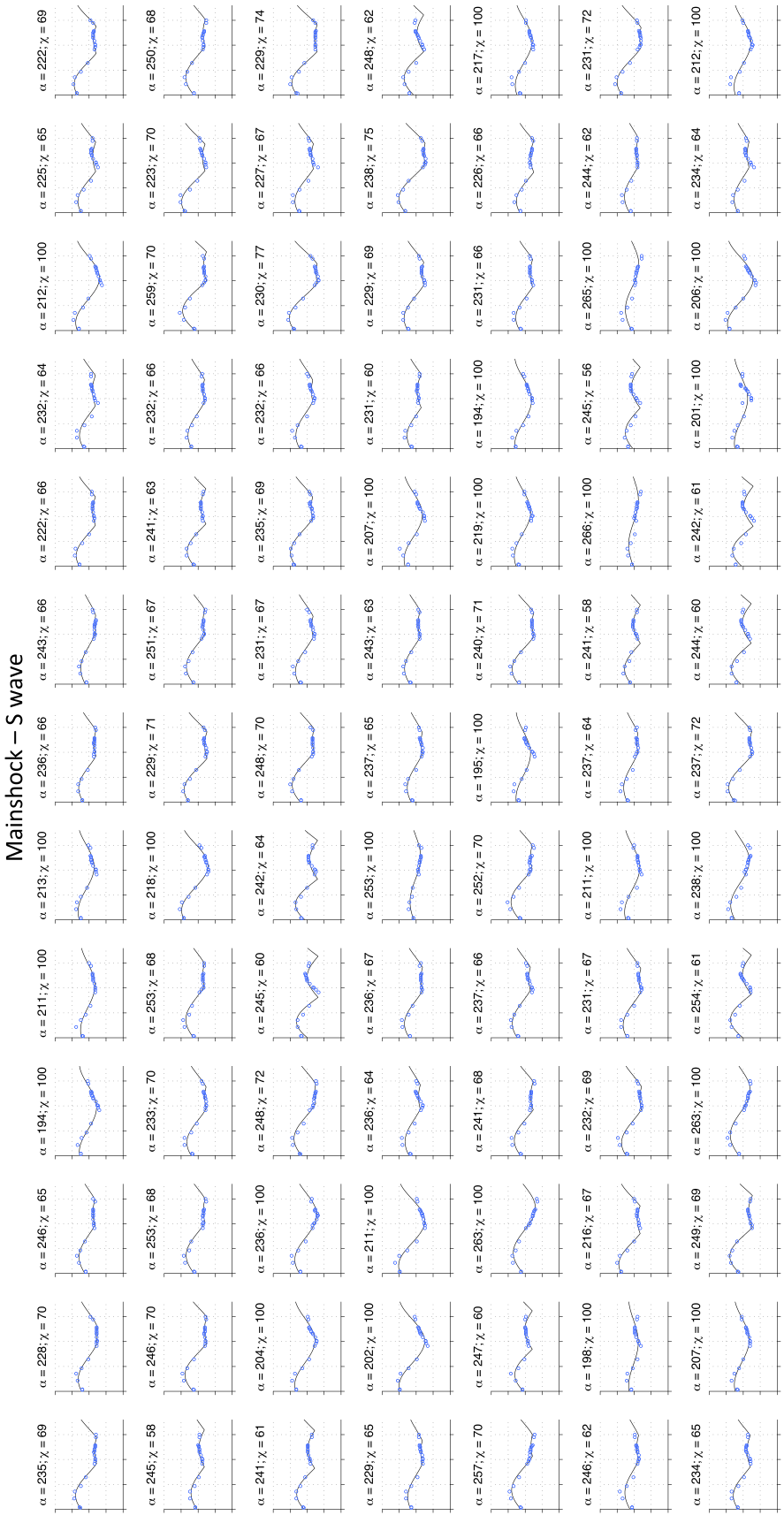

Figure 10. (b) Line source analysis for the synthetic ASTFs durations from the solution set of the mainshock for *S* wave.

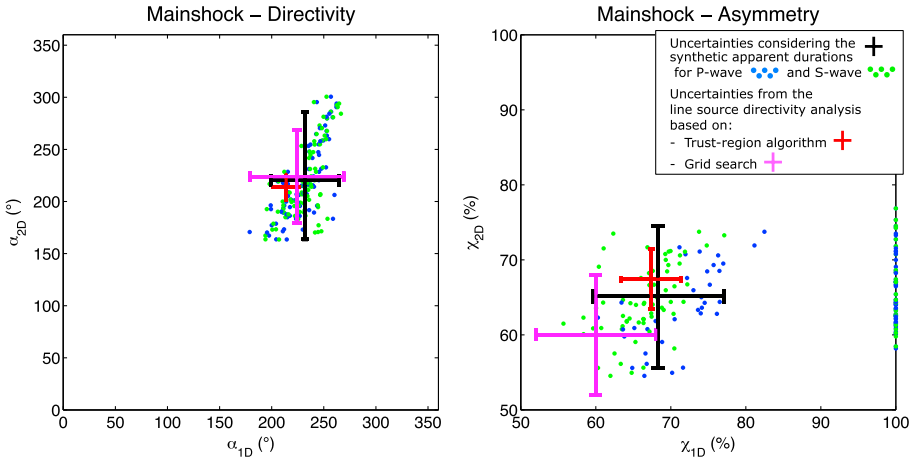

Figure 11. Comparison of 1-D and 2-D source parameterizations for the azimuth of rupture directivity (α) and the asymmetry (χ). Dots show the results from 2-D inversion with the directivity vectors of the solution set (see labels in Figure 7, note that α' is projected in the horizontal plane to obtain α) and the results from 1-D inversion considering the synthetic apparent durations for *P* wave (blue dots) and *S* wave (green dots) (see labels in Figure 10). Black crosses represent the uncertainties for these dots clouds taking into account a 95% confidence interval. Red and magenta crosses represent the uncertainties from the line source directivity analysis (trust-region algorithm and grid search, respectively) considering the observed apparent durations.

have been revealed by the model search. The percentage of asymmetry of the rupture, on the other hand, appears less well constrained, with viable solutions ranging from close to bilateral (~55%) to clearly asymmetric ruptures (~75% for the mainshock and ~80% for the foreshock).

Inversion for 1-D and 2-D source models involves very different numbers of parameters (four versus >100) with very different meaning. We complete this study with a consistency test between both methods. For this purpose, we reintroduce the solution set from Popperian fault slip inversion for the mainshock into line source analysis, performing an automatic picking of apparent source durations on predicted ASTFs. Duration is measured from the onset of synthetic ASTFs to the point where the signal has declined to 10% of the peak amplitude. This threshold emulates the picking strategy we adopted for data-derived ASTFs and avoids counting the asymptotic tail in many of the synthetic time functions, reflecting nonzero slip in peripheral parts of the models. Line source fits (Figure 10) reproduce well the azimuthal variability of apparent durations from 2-D inversion. Direction and percentage of directivity (α and χ, equation (2)) yield similar values as for direct line source inversion. To reconstruct line source parameters from 2-D inversion, we test equations (1) and (2) in parallel, retaining the solution with lowest misfit. We confirm the expected limitations in resolving highly asymmetric rupture (section 3), where we cannot guarantee convergence of the general bilateral search. For asymmetry around 70%, the secondary lobe of apparent durations becomes small, and from around 80% the solutions skip to apparent unilateral ruptures. The distribution of directivity values χ inferred from 2-D slip maps and corresponding line source simulations show relevant scatter and low correlation (Figure 11). The directivity direction α is recovered appropriately during line source postprocessing; however, the scatter of α observed in 2-D maps is slightly underestimated in line source inversion. Overall, uncertainties of α and χ are larger in 2-D inversion than in nonlinear trust-region 1-D inversion, and of the same order as 1-D inversion errors obtained from grid search (Figure 11). This means that our Popperian falsification criterion is a more conservative choice compared to 95% error estimates from the Jacobian, full waveforms of ASTFs are affected by more relevant uncertainty compared to measurements of apparent durations, or the 2-D parametrization is more prone to trade-offs that affect these parameters. As a footnote, from a Popperian perspective, all estimates of α and χ correspond to equally probable solutions, including those outside the 95% confidence interval in Figure 11.

6. Discussion and Conclusions

Assessing the resolution of finite or extended earthquake source inversion is important to support the consequent geological and physical interpretations. Minimization strategies that provide single best fitting

models do not inquire if a substantially different model could explain the data as well. Search approaches seem more appropriate to deal with the problem. Here we address the resolution of rupture directivity as one of the most important source properties. We can parameterize rupture directivity directly in inversion for a 1-D line source model, where azimuth, asymmetry, and speed of the rupture are the relevant parameters to adjust the observed variability of apparent source durations. Alternatively, we infer azimuth, asymmetry and rupture speed from inversions for full slip distributions in a 2-D fault model. Extended fault inversion involves a more general and realistic representation of the rupture model. Contrary to 1-D models, this allows using the full information contained in waveforms, instead of apparent durations alone. On the other hand, trade-offs among the large number of parameters become very unclear, and the inversion should come along with a suitable resolution test. We use a Popperian strategy for this purpose, leading to the falsification of a vast majority (98% to 99%) of pseudorandom trial distributions of fault slip on account of poor fit to the target ASTFs. The remainder of feasible models reveals ambiguities of the inverse problem through a multiplicity of solutions. Popperian inversion is different from Bayesian strategies [e.g., *Monelli and Mai*, 2008; *Minson et al*., 2014] in that we do not rank the likeliness of alternative solutions (beyond the classification into falsified and feasible models) but treat all feasible slip models as a set of coequal solutions to the inverse problem, available for postprocessing to infer azimuth and asymmetry of rupture.

We compare 1-D and 2-D source models for the Lorca M_w 5.2 mainshock, SE Spain. While the intrinsic nonuniqueness of seismic source inversion and derived directivity parameters acts at all scales and affects events of any magnitude, weak events are challenging because short wavelength data need to be analyzed. The azimuthal variability of apparent source durations for magnitude ~5 earthquakes is in the subsecond range, requiring a careful analysis in order to quantify directivity effects. Also, waveform modeling is typically beyond the capabilities of available Earth models, and thus, empirical Green's functions need to be used to isolate the signature of the source. ASTFs for the Lorca earthquakes show large azimuthal variability of apparent duration, indicating rupture directivity. Yet measured durations show scatter larger than picking errors, and no slip distribution can fully adjust the shape of mainshock ASTFs at stations toward the NE. Both observations suggest that deconvolved ASTFs suffer from shortcomings. ASTFs with more complicated shapes could possibly be explained by more complicated source models, but other seismic and geodetic data do not warrant a more general source parameterization [*Martínez-Díaz et al*., 2012; *De Michele et al*., 2013; *Rueda et al*., 2014; *Pro et al*., 2014]. We attribute the complexity of our longest ASTFs to spurious oscillations introduced in spectral division that breaks up continuous ASTFs into apparent sequences of overlapping pulses. The choice of the EGF earthquake, on the other hand, does not seem to be a source of complexity in this case, since ASTFs at NE stations show very similar shape when testing different EGFs [*López-Comino et al*., 2012].

Popperian extended fault inversion for the 2011 Lorca earthquakes (mainshock and foreshock) provides an ensemble of models with many general similarities and only relatively minor differences. In particular, the directivity rose diagram shows a smooth continuous distribution of directivity azimuths of individual models. No fundamental ambiguities, such as different number and configuration of main slip patches, were detected. The average model of the solution set is representative for the entire ensemble showing one asperity centered SW of the hypocenter in both earthquakes (Figure 8). The rupture propagation observed in 2-D inversion is consistent with directivity parameters obtained from line source inversion for the mainshock, except for differences in the resolution and perception of rupture asymmetry. Inversion of apparent source durations is intrinsically unable to distinguish between purely unilateral rupture and highly asymmetric bilateral rupture, because the apparent duration of the short leg of rupture propagation becomes shorter than the long leg for all azimuths. Popperian inversion for 2-D rupture patterns appears to be the most suitable strategy to estimate directivity in such circumstances. We generally advocate the practice of showing multiple alternative solutions of an inverse problem instead of a single best model.

For the Lorca mainshock, the apparent durations as well as the full shape of ASTFs are well fit by a moderately asymmetric bilateral rupture with ~70% of propagation along the long leg of the rupture surface. Predominant rupture propagation is in SW direction for both events, coincident with the direction to the city of Lorca (~N190°E). Clearly, this directivity has contributed to the large impact of the mainshock [*López-Comino et al*., 2012; *Morales et al*., 2013; *De Michele et al*., 2013; *Rueda et al*., 2014; *Pro et al*., 2014]. While rupture speed is unresolved in line source inversion, 2-D fault inversion provides better constrained estimates, suggesting fast rupture with 3.25 km/s for the mainshock and 2.75 km/s for the foreshock. Given the moderate asymmetry of the rupture, this suggests that the pronounced directivity effect in the

mainshock can be attributed mainly to the high rupture velocity $> 90\%\ v_S$. There is a difference between fault strike for the mainshock (N240°E [*López-Comino et al.*, 2012]) and directivity from line source inversion (N213° E from the trust-region algorithm and N224°E from grid search), indicating an anticlockwise rotation of horizontal directivity from the fault strike. The geometrical consequence of this rotation is an updip component of rupture propagation. The difference is significant in light of the 95% confidence limits of line source directivity from the trust-region algorithm (±12°); however, the line source grid search suggests that models without updip propagation also would yield satisfactory fits to apparent duration of the ASTFs.

Our results are evidence of a high similarity in the rupture properties and kinematic behavior of the Lorca mainshock and foreshock. Directivity toward the city of Lorca is observed in both earthquakes. Relocations of the Lorca sequence put the largest earthquakes at the northeastern termination of the series, suggesting a scenario where aftershocks are triggered preferentially in the forward direction of the mainshock rupture propagation. Directivity is predicted from dynamic rupture simulations in bimaterial scenarios, representative of different materials brought into contact across the fault surface due to accumulated long-term fault slip [*Shi and Ben-Zion*, 2006; *Ampuero and Ben-Zion*, 2008]. *Niemeijer and Vissers* [2014] suggest that the spatial variation of the frictional properties along the Alhama de Murcia fault was an important factor that controlled the spread of these movements, so these similarities may not be fortuitous. The directivity effects in the 2011 earthquakes could anticipate the kinematic behavior for future events with higher magnitude on the fault.

Acknowledgments
We are grateful to IGN, University of Alicante (AFON), and ROA/UCM/Geofon (CART) for providing high-quality seismic data from their stations. Martin Mai kindly provided codes for generating stochastic slip maps. We received financial support through project CGL2015-67130-C2-2-R Mineco/Feder, UE, and Junta de Andalucía research group RNM 104. A.M.G.F. thanks funding by the European Commission's Initial Training Network project QUEST (contract FP7 PEOPLE-ITN-2008-238007, www.quest-itn.org) and from project AQUAREL funded by FCT (PTDC/CTE-GIX/116819/2010), Portuguese Ministry of Education and Science. The data for this paper are available by contacting the corresponding author at jmorales@ugr.es.

References

Alguacil de la Blanca, G., F. Vidal Sánchez, D. Stich, F. Mancilla Pérez, J. A. López-Comino, J. Morales Soto, and M. Navarro Bernal (2012), Parámetros de la fuente y del movimiento del suelo del terremoto de Lorca de 2011, *Física de la Tierra*, *24*, 41–69.

Ampuero, J. P., and Y. Ben-Zion (2008), Cracks, pulses and macroscopic asymmetry of dynamic rupture on a bimaterial interface with velocity-weakening friction, *Geophys. J. Int.*, *173*, 674–692.

Andrews, D. J., and R. A. Harris (2005), The wrinkle-like slip pulse is not important in earthquake dynamics, *Geophys. Res. Lett.*, *32*, L23303, doi:10.1029/2005GL023996.

Benioff, H. (1955), *Mechanism and Strain Characteristics of the White Wolf Fault as Indicated by the Aftershock Sequence*, *Calif. Div. Mines Bull.*, vol. 171, pp. 199–202.

Ben-Menahem, A. (1961), Radiation of seismic surface-waves from finite moving sources, *Bull. Seismol. Soc. Am.*, *51*(3), 401–435.

Beresnev, I. A. (2003), Uncertainties in finite-fault slip inversions: To what extent to believe? (A critical review), *Bull. Seism. Soc. Am.*, *93*(6), 2445–2458.

Boatwright, J., and D. M. Boore (1982), Analysis of the ground accelerations radiated by the 1980 Livermore Valley earthquakes for directivity and dynamic source characteristics, *Bull. Seismol. Soc. Am.*, *72*, 1843–1865.

Boatwright, J., and M. Cocco (1996), Frictional constraints on cristal faulting, *J. Geophys. Res.*, *101*, 13,895–13,909, doi:10.1029/96JB00405.

Boore, D. M., and W. B. Joyner (1978), The influence of rupture incoherence on seismic directivity, *Bull. Seismol. Soc. Am.*, *68*, 283–300.

Brietzke, G. B., A. Cochard, and H. Igel (2009), Importance of Bimaterial Interfaces for Earthquake Dynamics and Strong Ground Motion, *Geophys. J. Int.*, *178*, 921–938.

Caldeira, B., M. Bezzeghoud, and J. F. Borges (2010), DIRDOP: A directivity approach to determining the seismic rupture velocity vector, *J. Seismol.*, *14*, 565–600.

Cesca, S., S. Heimann, and T. Dahm (2011), Rapid directivity detection by azimuthal amplitude spectra inversion, *J. Seismol.*, *15*, 147–164.

Coleman, T., and Y. Li (1994), On the convergence of reflective Newton methods for large-scale nonlinear minimization subject to bounds, *Math. Program.*, *67*, 189–224.

Coleman, T., and Y. Li (1996), An interior, trust region approach for nonlinear minimization subject to bound, *SIAM J. Optim.*, *6*, 418–445.

Courboulex, F., A. Dujardin, M. Vallée, B. Delouis, C. Sira, A. Deschamps, L. Honoré, and F. Thouvenot (2013), High frequency directivity effect for an M_w 4.1 earthquake, widely felt by the population in Southeastern France, *Bull. Seismol. Soc. Am.*, *103*, 3347–3353.

Custódio, S., P. C. Liu, and R. J. Archuleta (2005), The 2004 M_w 6.0 Parkfield, California, earthquake: Inversion of near-source ground motion using multiple data sets, *Geophys. Res. Lett.*, *32*, L23312, doi:10.1029/2005GL024417.

De Michele, M., P. Briole, D. Raucoules, A. Lemoine, and A. Rigo (2013), Revisiting the shallow M_w 5.1 Lorca earthquake (southeastern Spain) using C-band InSAR and elastic dislocation modelling, *Remote Sens. Lett.*, *4*(9), 863–872.

González, P. J., K. F. Tiampo, M. Palano, F. Cannavó, and J. Fernández (2012), The 2011 Lorca earthquake slip distribution controlled by groundwater crustal unloading, *Nat. Geosci.*, *5*, 821–825.

Hartzell, S. H. (1978), Earthquake aftershocks as Green's functions, *Geophys. Res. Lett.*, *5*, 1–4, doi:10.1029/GL005i001p00001.

Hartzell, S. H., and T. H. Heaton (1983), Inversion of strong ground motion and teleseismic waveform data for the fault rupture history of the 1979 Imperial Valley, California, earthquake, *Bull. Seismol. Soc. Am.*, *73*, 1553–1583.

Hartzell, S., P. Liu, C. Mendoza, C. Ji, and K. M. Larson (2007), Stability and uncertainty of finite-fault slip inversions: Application to the 2004 Parkfield, California, earthquake, *Bull. Seismol. Soc. Am.*, *97*(6), 1911–1934.

Haskell, N. A. (1964), Total energy and energy spectral density of elastic wave radiation from propagating faults, *Bull. Seism. Soc. Am.*, *54*, 1811–1841.

Kane, D. L., P. M. Shearer, B. P. Goertz-Allmann, and F. L. Vernon (2013), Rupture directivity of small earthquakes at Parkfield, *J. Geophys. Res. Solid Earth*, *118*, 212–221, doi:10.1029/2012JB009675.

Kikuchi, M., and H. Kanamori (1982), Inversion of complex body waves, *Bull. Seismol. Soc. Am.*, *72*, 491–506.

Lengliné, O., and J.-L. Got (2011), Rupture directivity of microearthquake sequences near Parkfield, California, *Geophys. Res. Lett.*, *38*, L08310, doi:10.1029/2011GL047303.

Ligorría, J. P., and C. J. Ammon (1999), Iterative deconvolution and receiver-function estimation, *Bull. Seism. Soc. Am.*, *89*, 1395–1400.

López-Comino, J. A., F. Mancilla, J. Morales, and D. Stich (2012), Rupture directivity of the 2011, M_w 5.2 Lorca earthquake (Spain), *Geophys Res Lett*, *39*, L03301, doi:10.1029/2011GL050498.

López-Comino, J. A., D. Stich, A. M. G. Ferreira, and J. Morales (2015), Extended fault inversion with random slipmaps: A resolution test for the 2012 M_w 7.6 Nicoya, Costa Rica earthquake, *Geophys. J. Int*, *202*, 77–93.

Mai, P. M., and G. C. Beroza (2002), A spatial random-field model to characterize complexity in earthquake slip, *J. Geophys. Res.*, *107*(B11), 2308, doi:10.1029/2001JB000588.

Martínez Díaz, J. J. (1998), Neotectónica y Tectónica Activa del sector centrooccidental de Murcia y Sur de Almería, Cordillera Bética (España), PhD thesis, Univ. Complutense de Madrid, p. 466.

Martínez-Díaz, J. J. (2002), Stress field variety related to fault interaction in a reverse oblique-slip fault: The Alhama de Murcia Fault, Betic Cordillera, Spain, *Tectonophysics*, *356*, 291–305, doi:10.1016/S0040-1951(02)00400-6.

Martínez-Díaz, J. J., M. Bejar-Pizarro, J. A. Álvarez-Gómez, F. Mancilla, D. Stich, G. Herrera, and J. Morales (2012), Tectonic and seismic implications of an intersegment rupture. The damaging May 11th 2011 M_w 5.2 Lorca, Spain, earthquake, *Tectonophysics*, *546–547*, 28–37.

Masana, E., J. J. Martínez-Díaz, J. L. Hernández-Enrile, and P. Santanach (2004), The Alhama de Murcia fault (SE Spain), a seismogenic fault in a diffuse plate boundary: Seismotectonic implications for the Ibero- Magrebian region, *J. Geophys. Res.*, *109*, B01301, doi:10.1029/2002JB002359.

McGuire, J. J., L. Zhao, and T. H. Jordan (2002), Predominance of unilateral rupture for a global catalog of large earthquakes, *Bull. Seismol. Soc. Am.*, *92*, 3309–3317.

Minson, S. E., M. Simons, J. L. Beck, F. Ortega, J. Jiang, S. E. Owen, A. W. Moore, A. Inbal, and A. Sladen (2014), A Bayesian approach to finite fault earthquake modeling. II: Application to the Great 2011 Tohoku-Oki earthquake, *Geophys. J. Int.*, *198*(2), 922–940, doi:10.1093/gji/ggu170.

Miyake, H., T. Iwata, and K. Irikura (2001), Estimation of rupture propagation direction and strong motion generation area from azimuth and distance dependence of source amplitude spectra, *Geophys. Res. Lett.*, *28*, 2727–2730, doi:10.1029/2000GL011669.

Monelli, D., and P. M. Mai (2008), Bayesian inference of kinematic earthquake rupture parameters through fitting of strong motion data, *Geophys. J. Int.*, *173*(1), 220–232.

Morales, J., J. V. Cantavella, F. L. Mancilla, L. Lozano, D. Stich, E. Herraiz, J. B. Martin, J. A. López-Comino, and J. M. Martinez-Solares (2013), The 2011 Lorca seismic series: Temporal evolution, faulting parameters and hypocentral relocation, *Bull. Earthquake. Eng.*, *12*, 1871–1888, doi:10.1007/s10518-013-9476-x.

Niemeijer, A. R., and R. L. M. Vissers (2014), Earthquake rupture propagation inferred from the spatial distribution of fault rock frictional properties, *Earth Planet. Sci. Lett.*, *396*, 154–164.

Olson, A. H., and R. J. Apsel (1982), Finite faults and inverse theory with applications to the 1979 Imperial Valley earthquake, *Bull. Seismol. Soc. Am.*, *72*, 1969–2001.

Pro, C., E. Buforn, S. Cesca, C. Sanz de Galdeano, and A. Udías (2014), Ruptures process of the Lorca (southeast Spain) 11 May 2011 (M_w = 5.1) earthquake, *J. Seismol.*, *18*, 481–495.

Rueda, J., D. Dreger, R. M. García Blanco, and J. Mezcua (2014), Directivity detection and source properties of the 11 May 2011 M_w 5.2 Lorca, Spain, earthquake, *Bull. Seismol. Soc. Am.*, *104*(4), 1735–1749, doi:10.1785/0120130143.

Santoyo, M. A. (2013), Finite fault analysis and near-field dynamic strain and rotation estimates due to the 11/05/2011 (M_w 5.2) Lorca earthquake, south-eastern Spain, *Bull. Earthquake. Eng.*, *12*, 1855–1870, doi:10.1007/s10518-013-9492-x.

Seekins, L. C., and J. Boatwright (2010), Rupture directivity of moderate earthquakes in Northern California, *Bull. Seismol. Soc. Am.*, *100*, 1107–1119, doi:10.1785/0120090161.

Shi, Z., and Y. Ben-Zion (2006), Dynamic rupture on a bimaterial interface governed by slip-weakening friction, *Geophys. J. Int.*, *165*, 469–484, doi:10.1111/j.1365-246X.2006.02853.x.

Smith, G. P., and G. Ekström (1997), Interpretation of earthquake epicenter and CMT centroid locations, in terms of rupture length and direction, *Phys. Earth Planet. Interiors*, *102*, 123–132.

Somerville, P. G. (2003), Magnitude scaling of the near fault rupture directivity pulse, *Phys. Earth Planet. Int.*, *137*, 201–212.

Somerville, P. G., N. F. Smith, R. W. Graves, and N. A. Abrahamson (1997), Modification of empirical strong ground motion attenuation relations to include the amplitude and duration effects of rupture directivity, *Seismol. Res. Lett.*, *68*, 199–222.

Warren, L. M., and P. M. Shearer (2006), Systematic determination of earthquake rupture directivity and fault planes from analysis of long-period *P*-wave spectra, *Geophys. J. Int.*, *164*, 46–62.

Weston, J., A. M. G. Ferreira, and G. J. Funning (2012), Systematic comparisons of earthquake source models determined using InSAR and seismic data, *Tectonophysics*, *532-535*, 61–81, doi:10.1016/j.tecto.2012.02.001.